

Molecular gas in NUClei of GALaxies (NUGA)

VIII The Seyfert 2 NGC 6574

E. Lindt-Krieg^{1,2}, A. Eckart^{1,3}, R. Neri², M. Krips⁴, J.-U. Pott^{1,5}, S. García-Burillo⁶, F. Combes⁷

¹ Universität zu Köln, 1.Physikalisches Institut, Zülpicher Strasse 77, 50937 Köln, Germany

² Institut de Radio-Astronomie Millimétrique (IRAM), 300 rue de la Piscine, 38406 St. Martin-d'Hères, France

³ Max-Planck-Institut für Radioastronomie, Auf dem Hügel 69, 53121 Bonn, Germany

⁴ Smithsonian Astrophysical Observatory (SAO), Submillimeter Array (SMA)645, North A'Ohoku Place, 96720 Hilo, USA

⁵ W.M. Keck Observatory, 65-1120 Mamalahoa Hwy, Kamuela, HI 96743, USA

⁶ Observatorio Astronómico Nacional (OAN), Alfonso XII, 3, 28014 Madrid, Spain

⁷ Observatoire de Paris, LERMA, 61 Av. de l'Observatoire, 75014 Paris, France

Received 17. Aug. 2007; accepted 2. Nov. 2007

ABSTRACT

Within the frame of the NUClei of GALaxies (NUGA) project, we have determined the distribution and kinematics of the molecular gas within the central kpc with high spatial resolution (100-150pc), for a sample of active galaxies. The goal is to study the gas-fueling mechanisms in AGN.

We present interferometric observations of $^{12}\text{CO}(1-0)$ and $^{12}\text{CO}(2-1)$ line emission from the Seyfert 2 galaxy NGC 6574, obtained with the IRAM Plateau de Bure Interferometer (PdBI). These data have been combined with 30m mapping data in these lines to correct for the flux resolved by the interferometer. At an angular resolution of $0.7''$ ($\equiv 110\text{pc}$), the $^{12}\text{CO}(2-1)$ emission is resolved into an inner disk with a radius of 300 pc.

The molecular gas in NGC 6574 is primarily distributed in four components: nucleus, bar, spiral arms - winding up into a pseudo-ring - and an extended underlying disk component. For the overall galaxy host, we find a $^{12}\text{CO}(2-1)$ to $^{12}\text{CO}(1-0)$ line ratio of ~ 0.3 indicative of cold or sub-thermally excited gas. For the nucleus, this ratio is close to unity, indicating emission from dense and warm molecular gas. Modeling the gas kinematics with elliptical orbits shows that the molecular gas in the differentially rotating disk of NGC 6574 is strongly influenced by the presence of a stellar bar. The nuclear component shows an extension toward the southeast that may be an indication of the lopsidedness of the nuclear gas distribution.

We computed the gravity torques exerted from the stellar bar on the gas, deriving the gravitational potential from near-infrared images, and weighting the torques by the CO distribution. We find negative torques for the gas inside the ring, since the gas aligned with the bar has a slight advance phase shift, leading the bar. This means that gas is flowing in towards the center, at least down to 400pc in radius, which can explain the observed high nuclear gas concentration. This concentration corresponds to a possible inner Lindblad resonance of the bar, according to the measured rotation curve. The gas has been piling up in this location quite recently, since no starburst is been observed yet.

Key words. galaxies: individual: NGC 6574 - galaxies: active - galaxies: kinematics and dynamics

1. Introduction

The study of interstellar gas in the nuclei of galaxies is a fundamental for understanding nuclear activity through fueling the active galactic nuclei (AGN) and their relation to circum-nuclear star formation. Some studies claim that pure gaseous density waves (spirals, bars, warps, or lopsided instabilities) may be driving gas inflow towards the AGN (Heller & Shlosman 1994; Elmegreen et al. 1998; Regan & Mulchaey 1999). While such dynamical perturbations are responsible for the infall of gas on large scales, the processes responsible for

removing angular momentum on small scales (sub-kpc) have not been understood very well yet.

Different scenarios have been introduced trying to explain this phenomenon, such as nested bars (e.g., Friedli & Martinet 1993, spirals e.g., Martini & Pogge 1999,) warped nuclear disks (Schinnerer et al. 2000a,b), and lopsidedness or $m=1$ instabilities (Kormendy & Bender 1999; García-Burillo et al. 2000). Most of the gas within the central kiloparsec of spiral galaxies is in the molecular phase, while the atomic gas is deficient there.

This makes CO lines the best tracers of nuclear gas dynamics in the nuclear interstellar medium. High-resolution ($1''$ - $2''$)

maps of the molecular component in the centers of galaxies are required to model these nuclei within the Nuclei of GALaxies (NUGA) project. The NUGA project aims at establishing a high angular resolution ($\approx 0.5'' - 1''$) and high-sensitivity CO survey of twelve objects. It covers the whole sequence of activity types: Seyfert 1, Seyfert 2, LINERs, and transition objects, and it comprises 12 objects as a core sample and a total of about 30 objects as an extended sample. The survey is being carried out with the IRAM Plateau de Bure mm-Interferometer (PdBI) in France, because it offers the best combination of sensitivity and resolution, both crucial for this project. A more detailed description of the NUGA project is given in Paper I by García-Burillo et al. (2003).

Previous surveys of molecular gas in active galaxies have been carried out by other groups (Heckman et al. 1989; Meixner et al. 1990; Vila-Vilaro et al. 1998; Sakamoto et al. 1999a,b), but have had insufficient spatial resolution ($4-7''$) to resolve the nuclear disk structures, or else were limited to small samples (Tacconi et al. 1997; Baker 2003). Besides case-by-case analyses and simulations of each object of the sample (García-Burillo et al. 2003; Combes et al. 2004; Krips et al. 2005; García-Burillo et al. 2005), the collected data of the NUGA project also provides an initial statistical basis for studying different mechanisms that may be responsible for gas flow toward the nuclei or may account for further accretion inward.

This paper describes the distribution and dynamics of molecular gas in NGC 6574, one of the galaxies belonging to the NUGA survey. NGC 6574 is a Seyfert 2 galaxy of Hubble type SB(s)bc, at a distance of 33 Mpc. This results in a spatial scale of ~ 160 pc per arcsecond. Its main characteristic is a symmetric structure with two spiral arms to the north and south of the center, nested on a small bar within the central $8''$. Kotilainen et al. (2000) present high spatial-resolution, near-infrared broad-band JHK and Br γ $2.166 \mu\text{m}$ and H $_2$ 1-0 S(1) $2.121 \mu\text{m}$ emission line images of the circum nuclear star-formation ring. The overall near-infrared and radio morphologies (see Laine et al. 2006) generally agree with each other. The observed H $_2$ /Br γ ratio indicates that the main excitation mechanism of the molecular gas is UV radiation from hot young stars. Shocks are likely to contribute only in a few regions. To explain the NIR data, Kotilainen et al. (2000) prefer the model of an instantaneous burst of star formation with an upper mass cutoff of $M_u = 100 M_\odot$ occurring $\sim 6-7$ Myr ago. An analysis of the molecular gas distribution at an angular resolution of about $4''$ in the $^{12}\text{CO}(1-0)$ line is presented by Sakamoto et al. (1999ab). They find a prominent CO peak of 1 kpc diameter at the center of the galaxy on a smooth gas disk with two gas/dust lanes that extend about 2 kpc from the central peak to east and west at a PA of $\sim 105^\circ$. From the tips of this gaseous bar, spiral arms start to form a ring-like structure.

In this paper we analyze data obtained with the IRAM PdBI and the 30 m single-dish telescope in the $^{12}\text{CO}(1-0)$ and $^{12}\text{CO}(2-1)$ lines. The angular resolution we obtained in the combined data set is about $2''$ and $0.7''$. We describe the molecular gas distribution and kinematics with elliptical bar orbits, to account for the influence of the stellar bar potential in the nucleus of NGC 6574. In Section 2 we describe the CO obser-

vations and in Section 3 we present the first results. The kinematic model and its results are discussed in Section 4. Gravity torques and the nature of gas flows are derived in Section 5, while Section 6 concludes.

2. Observations and data reduction

In this section we present the ^{12}CO observations with the IRAM 30m single dish, with the IRAM PdBI, including the short-spacing correction.

2.1. ^{12}CO observations with the IRAM 30m single dish

We performed IRAM 30m observations in a 7×7 raster pattern with $10''$ spacing in August 2005, in order to add the short spacings and to estimate the flux density filtered out by the interferometric observations. We used 4 SIS receivers to observe simultaneously at the redshifted frequencies of the $^{12}\text{CO}(1-0)$ and the $^{12}\text{CO}(2-1)$ lines, thereby assuming the LSR velocity of NGC6574 of 2282 km s^{-1} . For each line, a 4 MHz channel filter bank was used with a velocity resolution smoothed to about 10 km s^{-1} in order to improve the signal-to-noise ratios of the individual spectra. The 4 MHz filter bank consists of nine units. Each unit has 256 channels which covers a total bandwidth of 1 GHz. At 115 GHz and 230 GHz, the HPBW is $21.5''$ and $10.75''$, respectively. The parameters for the two observing runs are summarized in Table 1. We used the wobbler switch mode with a 6 s cycle and a throw of $240''$. With the forward efficiency F_{eff} , the main-beam efficiency is $B_{eff} = F_{eff} \times T_A^* / T_{mb} = 0.74$ at 115 GHz and 0.53 at 230 GHz. The typical system temperature varied between 200 and 450 K at both frequencies. The pointing was checked regularly on continuum sources and the accuracy was consistent to $3''$ rms achieved by Greve et al. (1996). The total bandwidth available was 512 MHz at 115 GHz and 230 GHz, corresponding to 1330 km s^{-1} and 666 km s^{-1} , respectively. The data reduction and analysis were done with the GILDAS package (e.g. Guilleoteau & Lucas 2000). For the short-spacing correction and further investigations, only the 4 MHz filter bank was used.

Parameters	CO(1-0)	CO(2-1)
central coordinates	RA = $18^h 11^m 51.3^s$, DEC = $+14^\circ 58' 52.1''$	
backends	4 MHz filter bank/autocorrelator	
redshift z	0.007662	
sky frequency [MHz]	114.400	228.798
beam size [arcsec]	21.50	10.75
beam efficiency B_{eff}	0.739	0.527
forward efficiency F_{eff}	0.95	0.91
total obs. time [sec]	14994	14994
Nr. of positions	49	49
Nr. of scans	294	294

Table 1. Parameters of the observing run with IRAM 30m single dish.

2.2. ^{12}CO observations with IRAM PdBI

We observed the emission of the J=1-0 and J=2-1 lines of ^{12}CO in a single field centered at the radio position of the AGN (i.e., $\alpha_{2000}=18^{\text{h}}11^{\text{m}}51.3^{\text{s}}$ and $\delta_{2000}=14^{\circ}58'52.1''$) in NGC 6574 with the IRAM Plateau de Bure interferometer (PdBI) in April 2002 (D configuration), in November 2003 (C configuration) and February 2004 (A and C configurations). The six 15 m antennae were equipped with dual-band SIS receivers. The spectral correlators were centered at 114.400 GHz and 228.798 GHz, respectively, with three correlator units covering a total bandwidth of 400 MHz at each frequency. The difference between LSR and heliocentric velocities is 12 km s^{-1} , therefore the observations were centered on $v_{\text{hel}} = 2282 \text{ km s}^{-1}$. The correlator was regularly calibrated by a noise source inserted in the IF system.

The bandpass calibrator was 3C 273 or MWC349, while the phase and amplitude calibration were performed on the nearby quasars 1923+210 and 1749+096, depending on the data set. Flux densities were calibrated relative to CRL618 and MWC349. The data were phase calibrated in the antenna-based mode. The frequencies were centered on the redshifted $^{12}\text{CO}(1-0)$ line in the USB at 3 mm and on the redshifted $^{12}\text{CO}(2-1)$ line in the LSB at 1 mm. For each line, the total bandwidth was 400 MHz and the spectral resolution 1.25 MHz. The integration time for the central pointing amounts to ~ 16 hrs on the source. The water vapor ranged between 4 and 10 mm (i.e., opacities of $\sim 0.2-0.3$) resulting in system temperatures of approximately 200-300 K on average.

The flux densities of the primary calibrators were determined from IRAM measurements and taken as input for deriving the absolute flux density scales for our visibilities, estimated to be accurate to 10%. The parameters for the four observing runs are summarized in Table 2.

The data reduction and mapping was performed using the GILDAS software. Data cubes with 512×512 spatial pixels ($0.25''/\text{pixel}$) were created with velocity planes separated by 5 km s^{-1} (for PdBI alone, and by 10 km s^{-1} for the short-spacing corrected data). The cubes were cleaned with the Clark (1980) method for $^{12}\text{CO}(1-0)$ data and with MX for $^{12}\text{CO}(2-1)$ data. As synthesized clean beams we used a $2.48'' \times 1.69''$ Gaussian with $\text{PA} = 26^{\circ}$ at 3 mm and a $0.93'' \times 0.5''$ Gaussian with $\text{PA} = 12^{\circ}$ at 1 mm. The rms noise levels in the cleaned maps (at 5 km s^{-1} velocity resolution) are 3 mJy/beam and 6 mJy/beam for the $^{12}\text{CO}(1-0)$ and $^{12}\text{CO}(2-1)$ lines, respectively. No continuum emission was detected toward NGC 6574. The maps were corrected for primary beam attenuation.

Parameters	CO(1-0)	CO(2-1)
central coordinates	RA = $18^{\text{h}}11^{\text{m}}51.3^{\text{s}}$, DEC = $+14^{\circ}58'52.1''$	
redshift z	0.007662	
sky frequency [MHz]	114.400	228.798
beam size [arcsec]	2.48×1.69	0.91×0.48
position angle [degree]	26	12

Table 2. Parameters of the observing run with IRAM PdBI.

2.3. Short-spacing correction

Short spacings were included using the SHORT-SPACE task in the GILDAS software. To find the best compromise between good angular resolution and complete restoration of the missing extended flux, the weights attached to the 30m and PdBI data were varied. At the end, a factor of two was applied to

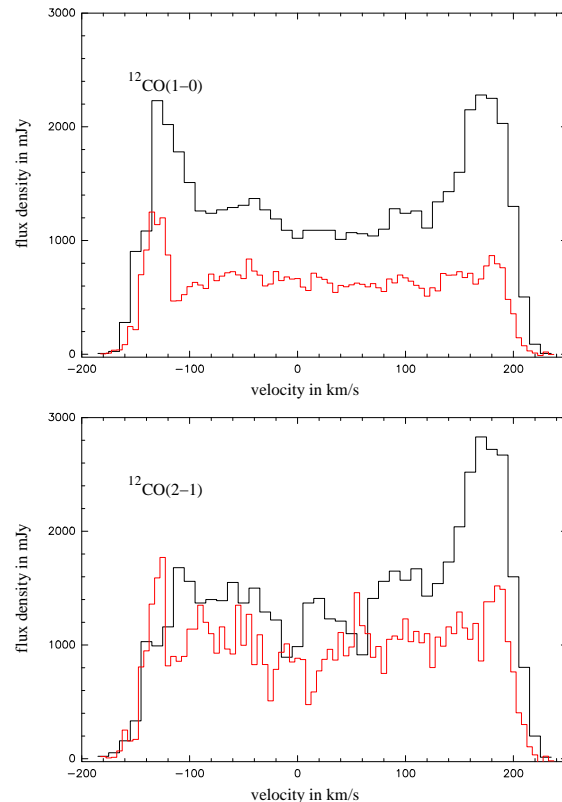


Fig. 1. The $^{12}\text{CO}(1-0)$ and $^{12}\text{CO}(2-1)$ line intensity derived from the PdBI data set (red) and the combined PdBI+30m data set (black). The spectra combine the information shown in the channel map in Fig. 2. The comparison shows the larger amount of extended emission for the $^{12}\text{CO}(1-0)$ line that is resolved by the interferometer. Both sets of spectra also demonstrate the asymmetry in flux density between the red and blue shifted part of the spectrum. The red side of the spectrum is brighter mostly in its extended emission.

the weights of the 30m data enabling us to recover more than 40% of the missing flux and to retain the angular resolution of $2.48'' \times 1.69''$ at PA of 26° for $^{12}\text{CO}(1-0)$ emission and $0.93'' \times 0.5''$ at PA of 12° for $^{12}\text{CO}(2-1)$ emission. The combined data sets were written to visibility tables, converted to maps using standard reduction procedures, and then deconvolved using the Clark algorithm. The weights were adjusted to get the same mean weights in the single-dish data as in the interferometer data in the u-v range of $1.25 D/\lambda$ to $2.5 D/\lambda$ ($D=15 \text{ m}$). All figures presented in this paper are done with short-spacing corrected data.

The line intensities and CO luminosities integrated over the entire linewidth of the full $\Delta v=370 \text{ km s}^{-1}$ extent of the com-

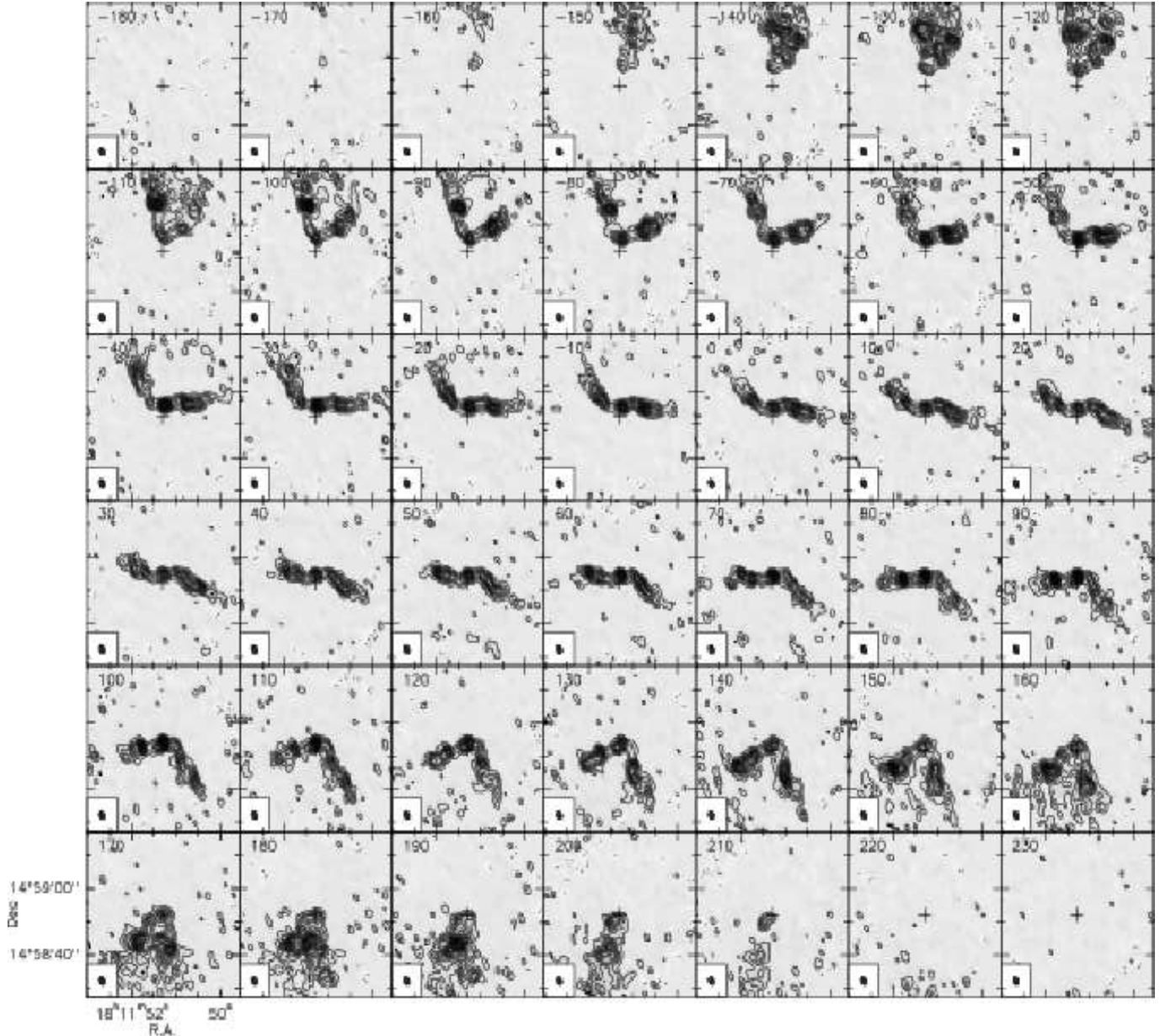


Fig. 2. $^{12}\text{CO}(1-0)$ velocity-channel maps observed with the PdBI and corrected through short-spacing by the 30m single dish in the nucleus of NGC 6574. The clean beam resulting from the observations is $2.48'' \times 1.69''$ at $\text{PA}=26^\circ$. It is plotted as a filled ellipse in the bottom left corner of each panel. We show a field of view of $55''$. The phase-tracking center is indicated by a cross at $\alpha_{2000} = 18^{\text{h}}11^{\text{m}}51.3^{\text{s}}$ and $\delta_{2000} = +14^\circ58'52.1''$. Velocity channels are displayed from $v = -180 \text{ km s}^{-1}$ to $v = 230 \text{ km s}^{-1}$ in steps of 10 km s^{-1} . Velocities are in LSR scale. Contour levels are 0.42σ , 0.84σ to 4.8σ in steps of 0.42σ , where the $1-\sigma$ rms is $\sigma=2.39 \text{ mJy beam}^{-1}$.

bin PdBI+30m map after correcting for primary beam response are listed in Table 3. Since these maps contain the entire galaxy, the corresponding quantities give information on the overall molecular excitation in NGC 6574. The difference between the integrated quantities for the $^{12}\text{CO}(1-0)$ line emission already indicate the presence of an extended disk component that is resolved out by the interferometer (see Fig. 1).

3. Results

In this section we first describe the morphology of NGC 6574 and show its kinematics, then estimate the gas masses and related parameters.

3.1. Morphology of the CO emission

In Fig. 2 we show the velocity-channel maps of the $^{12}\text{CO}(1-0)$ line emission in the central region of NGC 6574, with a velocity range of 410 km s^{-1} and a velocity resolution of 10 km s^{-1} .

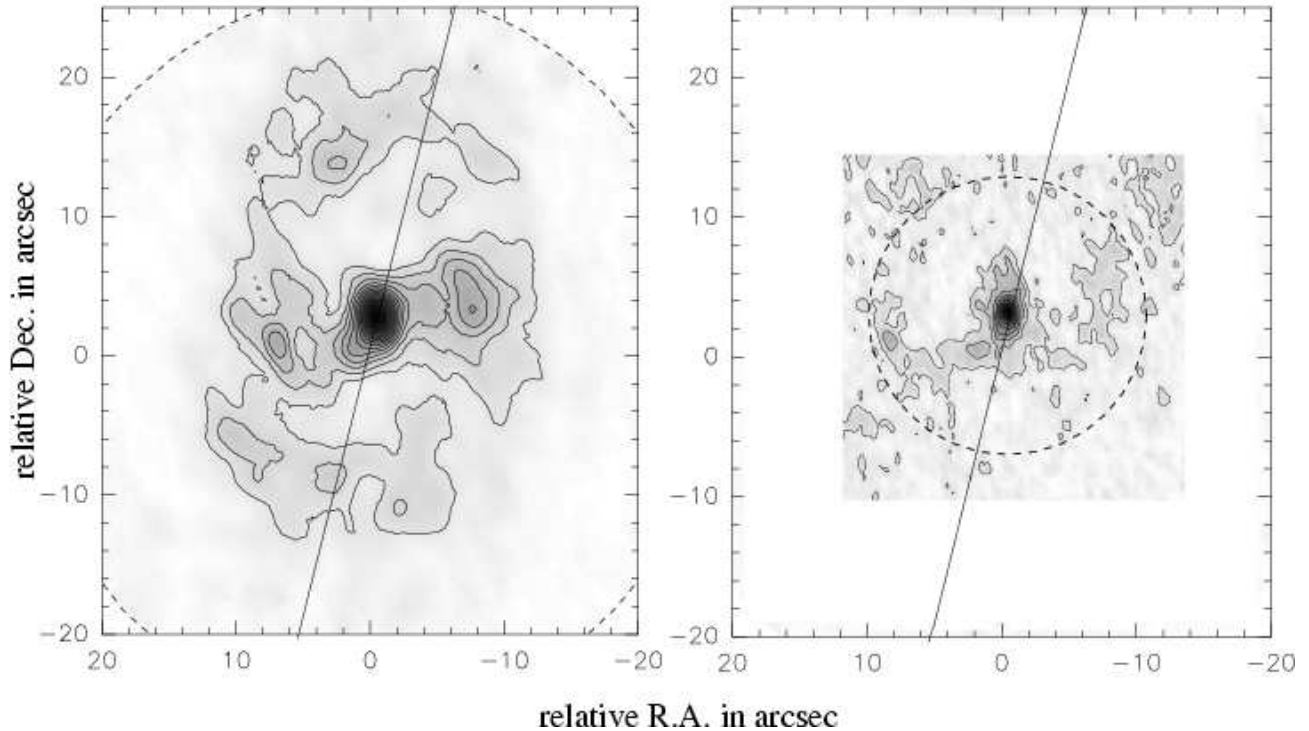


Fig. 3. Primary beam corrected integrated intensity maps for the $^{12}\text{CO}(1-0)$ (left) and $^{12}\text{CO}(2-1)$ (right) line emission. The straight lines at PA = 165° indicate the position of the major axis of NGC 6574 along and perpendicular to which we obtain position-velocity diagrams. The $^{12}\text{CO}(2-1)$ map is shown in the same frame as the $^{12}\text{CO}(1-0)$ map. The dashed circles outline the central regions that approximately include the FWHM areas of the PdBI primary beams at the two frequencies. For larger radii the map is too noisy. Inside that radius the nuclear emission as well as emission from the bar can be detected. This includes the tips of the bar at which the spiral arms start. Contour lines are 1, 2, 3, 4, ..., 16 Jy km/s /beam for $^{12}\text{CO}(1-0)$ and 1.8, 3.6, 5.4, 7.2, ... 15 Jy km/s /beam for $^{12}\text{CO}(2-1)$ line emission map, with beam sizes given in Table 2.

Line	I_{CO} Jy km $^{-1}$	L_{CO} K km $^{-1}$ pc 2
$^{12}\text{CO}(1-0)$		
PdBI	223 ± 9	6.43×10^8
PdBI + 30m	485 ± 15	13.5×10^8
$^{12}\text{CO}(2-1)$		
PdBI	360 ± 11	2.49×10^8
PdBI + 30m	540 ± 17	3.69×10^8

Table 3. Line intensities and CO luminosities integrated over the entire linewidth of the full $\Delta v = 370$ km s $^{-1}$ and the extent of the combined PdBI+30m map after correcting corrected for primary beam response (typical errors are of the order of 20%).

The typical ‘butterfly’ structure visible in the iso-velocity maps in Fig. 5 is the signature of a spatially resolved rotating disk. In the central $4''$ - $5''$ the location of the nuclear peak emission in the ^{12}CO emission also moves from the northern part of the channel map at the velocity of -170 km s $^{-1}$ to the southeast at the velocity of 220 km s $^{-1}$ with respect to the phase-tracking center of the map. The displacement of the nuclear component as a function of velocity shows that it is resolved, and it implies the rotation of the nuclear gas around the very center of NGC 6574. In the $^{12}\text{CO}(1-0)$ integrated intensity map shown in Fig. 3 (left), the molecular gas distribution reveals a regular

ring-like structure, with a mean angular diameter of $\sim 50''$ and the peak of the emission in the central $4''$ - $5''$. The integrated map was produced by averaging the channel maps over a total velocity width of 415 km s $^{-1}$ (from -180 to 235 km s $^{-1}$). For the $^{12}\text{CO}(1-0)$ emission, the ring consists of some molecular cloud complexes that appear to be connected to each other. They form the two spiral arms of NGC 6574 that start at a PA of $\sim 100^\circ$ and a projected radius of $r \sim 1.1$ kpc (1.55 kpc deprojected with an inclination of 45° - see below), near the end points of a prominent nuclear bar and extend out to radii of about $r \sim 2.4$ kpc towards the north and south, approximately along the major axis. A comparison to NIR images (Kotilainen et al. 2000) reveals that the position of the central, resolved CO source coincides to within less than $0.25''$ with that of the AGN. From the $^{12}\text{CO}(1-0)$ map in Fig. 3 (left) we estimate a gas bar PA of about $115^\circ \pm 5^\circ$, taking into account that the line emission on the western and eastern sides of the bar appear to be displaced by about $1''$ - $2''$ to the south and north, respectively. Our value of 115° is in reasonably agreement with the value of 105° (towards the western tip of the bar and derived from a lower resolution map) given by Sakamoto et al. (1999ab). It also apparently agrees with the NIR maps presented by Kotilainen et al. (2000). The NIR stellar bar has a PA of 105° , which means that our high-resolution CO maps are able to detect a slight advance phase shift between the stellar and gas bars, the latter leading

by about 10° . Kotilainen et al. (2000) also interpret the elongation of the nuclear component as a possible nuclear bar, with an orientation of $PA = 150^\circ$, however, this feature is not certain and could be due to projection effects, as the PA of the major axis is 165° . The CO spiral arms, starting at the end of the bar, mostly lie at the trailing edges of the nuclear bar. This particular geometry may determine the feeding budget for the gas in this region. The spiral arms and the central source are connected by a molecular gas bridge - the small bar. Contrary to $^{12}\text{CO}(1-0)$, the $^{12}\text{CO}(2-1)$ integrated emission is detected mainly inside the central component within the radius of $4''$ - $6''$, as shown in Fig. 3 (right). The maximum of the emission is concentrated at the center as well. While our $^{12}\text{CO}(2-1)$ map lacks sensitivity outside the central 500 pc of the disk, it does give a sharp image of the molecular gas distribution in the vicinity of the AGN. Also the tips of the nuclear bar in the eastern and western parts of the galaxy are indicated.

3.2. Kinematics of the molecular gas disk

The kinematics of the molecular gas are dominated by its motion in a rotating disk. In addition we see the influence of spiral arms and a bar potential. In Fig. 4 we show the position-velocity (p-v) plot along the major axis at $PA = 165^\circ$ and along the minor axis at $PA = 75^\circ$. By comparing the 30m and PdBI spectra extracted from the corresponding maps at the same positions, we find that there is some excess extended emission (as also suggested by Fig. 1), especially in the southern part of NGC 6574. Therefore both the PdBI and the 30m data indicate that the molecular gas emission is asymmetric with respect to v_{sys} , so the CO emission is preferentially redshifted (see Fig. 1). Our results agree well with the previous finding by Sakamoto et al. (1999ab), which were obtained at a lower resolution.

The position velocity diagram along the major axis shows the rotation curve that still has to be corrected for the inclination of the galactic disk. For both lines of ^{12}CO emission, the results are similar; however, differences between them can be found in the central $2''$. The p-v diagram of the $^{12}\text{CO}(1-0)$ line resolves the disk and nuclear region of the galaxy. There is some evidence of $^{12}\text{CO}(2-1)$ line emission at the very central position, although the diagram clearly shows that the emission at the systemic velocity is suppressed with respect to the emission arising at $0.5''$ to a $1''$ separation from the nucleus. This expresses itself in two emission clumps neighboring the central position and systemic velocity in the $^{12}\text{CO}(1-0)$ p-v diagram. This could hint at the existence of a small nuclear ring. The minor axis feature is a clear indication of non circular motion, expected in a bar, supporting the nuclear bar hypothesis. In the $^{12}\text{CO}(2-1)$ p-v diagram this contrast between the clumps is also visible on the major axis and reduced on the minor axis. However, the $^{12}\text{CO}(2-1)$ map has less sensitivity, due to its increased spatial resolution.

The distribution of the ^{12}CO emission, as well as the iso-velocity maps, also indicates a more complex molecular gas kinematics in the center of the galaxy. The iso-velocity map of $^{12}\text{CO}(1-0)$ and $^{12}\text{CO}(2-1)$ line emission were made from maps at the full angular resolution of $2.48'' \times 1.62''$ and $0.93'' \times 0.5''$,

respectively. In both cases we used equally spaced velocity channels with a velocity range from -170 to 220 km s^{-1} (see Fig. 5) with the central channel centered on the systemic velocity. The maps show the increase in velocities from north to south in both lines. The iso-velocity lines of the central $10''$ are parallel to each other but tilted by about 20° with respect to those of the outer disk sections of NGC 6574. This is a clear indication of the presence of spiral arms at the location of the bends between the iso-velocity contours and the influence of a barred potential that expresses itself in an overall tilt of the velocity field with respect to that of the molecular disk. While the $^{12}\text{CO}(1-0)$ line shows the velocity field for the whole galaxy (disk + nucleus), the $^{12}\text{CO}(2-1)$ line emission only allows us to derive the velocity field for the central $4'' \times 4''$ region. Here the overall orientation of the iso-velocity lines is similar to the $^{12}\text{CO}(1-0)$ but shown at a higher angular resolution - hence the influence of the barred potential is more pronounced.

3.3. Molecular gas masses

The velocity-integrated $^{12}\text{CO}(1-0)$ flux within the $\sim 50''$ primary beam of the combined IRAM PdBI/30m data is used to estimate molecular hydrogen masses. We use $I'_{\text{CO}}[\text{K km s}^{-1}] = 0.12 \times 10^{25} \cdot I_{\text{CO}}[\text{Jy km s}^{-1}] \cdot \nu^{-2}[\text{Hz}] \cdot \theta^{-2}[\text{''}]$, with the observing frequency ν and the beam size of the corresponding map θ . The column density of molecular hydrogen can be derived from I'_{CO} by assuming the validity of an average conversion factor $X = N(\text{H}_2)/I'_{\text{CO}} = 2.2 \times 10^{20} [\text{cm}^{-2} \text{K km s}^{-1}]$ (see e.g. Solomon & Barrett 1991):

$$N(\text{H}_2) = X \left[\frac{\text{cm}^{-2}}{\text{K km s}^{-1}} \right] \cdot I'_{\text{CO}}[\text{K km s}^{-1}] . \quad (1)$$

To estimate the molecular gas mass, the column density $N(\text{H}_2)$ then needs to be multiplied with an effective projected area A over which the CO line emission is distributed:

$$M_{\text{H}_2}[M_\odot] = 1.51 \times 10^{-14} \cdot N(\text{H}_2)[\text{cm}^{-2}] \cdot A[\text{kpc}^2] . \quad (2)$$

Including the relative contribution of helium and neutral atomic hydrogen, the total gas mass contained in the disk of NGC 6574 can be estimated via

$$M_{\text{gas}}[M_\odot] = 1.36 \cdot (M_{\text{H}_2} + M_{\text{H}_I}) , \quad (3)$$

with helium mass contained in the factor of 1.36.

The total dynamical mass of NGC 6574 is derived from the virial theorem by using the inclination-corrected circular velocity for a given radius via $M_{\text{dyn}}[M_\odot] = 232 \times v_{\text{rot}}^2(r)[\text{km s}^{-1}] \times r[\text{pc}]$. The error of the Keplerian dynamical mass due to the flatness of the mass distribution is at most 30% for an exponential disk (Binney & Tremaine 1987). All results are summarized in Table 4, separated into two components: the nucleus, which contains the flux of the inner $4''$, and the disk, containing the residual flux within the $50''$ of the integrated map. This central source contains a molecular gas mass of $\sim 10^8 M_\odot$. Estimated from the kinematics revealed by the $^{12}\text{CO}(1-0)$ line emission, the total dynamical mass of NGC 6574 contained within a radius of about $15''$ is $M_{\text{dyn}}[M_\odot] \sim 3.5 \times 10^{10}$. The molecular gas contributes about 6% to the dynamical mass in the inner 6 kpc. This is a typical value for a moderately gas-rich barred spiral.

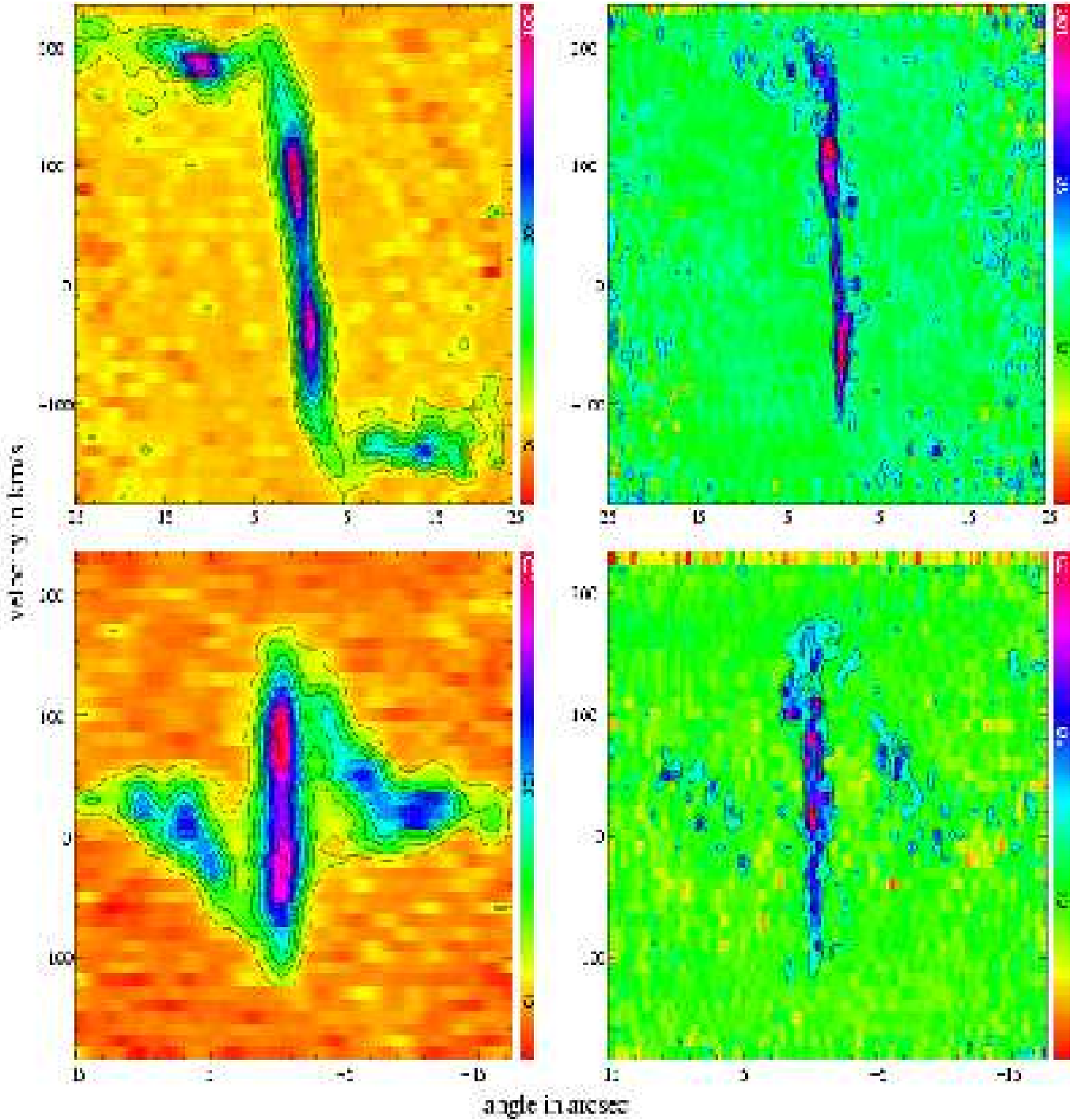


Fig. 4. Position-velocity diagrams of $^{12}\text{CO}(1-0)$ and $^{12}\text{CO}(2-1)$ along the major axis at 165° (*upper panels*) and minor axis at 75° (*lower panels*). For the top and bottom diagrams, the left side corresponds to the approximate south and east directions, respectively. The color bar gives the relative peak intensities in percent, with 0, 50, and 100% levels indicated just below the corresponding marks or the top of the bar. From the top left to the bottom right graph the contour lines are equidistantly spaced in 7, 17, 10, and 17% of the peak intensity, respectively.

3.4. CO line ratios

Comparison of the two CO line maps, at the same resolution and with the same spatial frequency sampling, can yield information about the excitation condition of the gas. We studied the variation in the $^{12}\text{CO}(2-1)/^{12}\text{CO}(1-0)$ ratio in areas with significant emission levels in both lines, i.e. in channels with veloci-

ties from -180 to 220 km s^{-1} . Within the $20.5''$ primary beam, the $^{12}\text{CO}(2-1)$ map was first smoothed to the spatial resolution of the $^{12}\text{CO}(1-0)$ map to assure that the two lines sample identical regions. The maps were then corrected for primary beam attenuation. We find a nuclear $^{12}\text{CO}(2-1)/^{12}\text{CO}(1-0)$ line ratio close to unity and an off-nuclear ratio around 0.2.

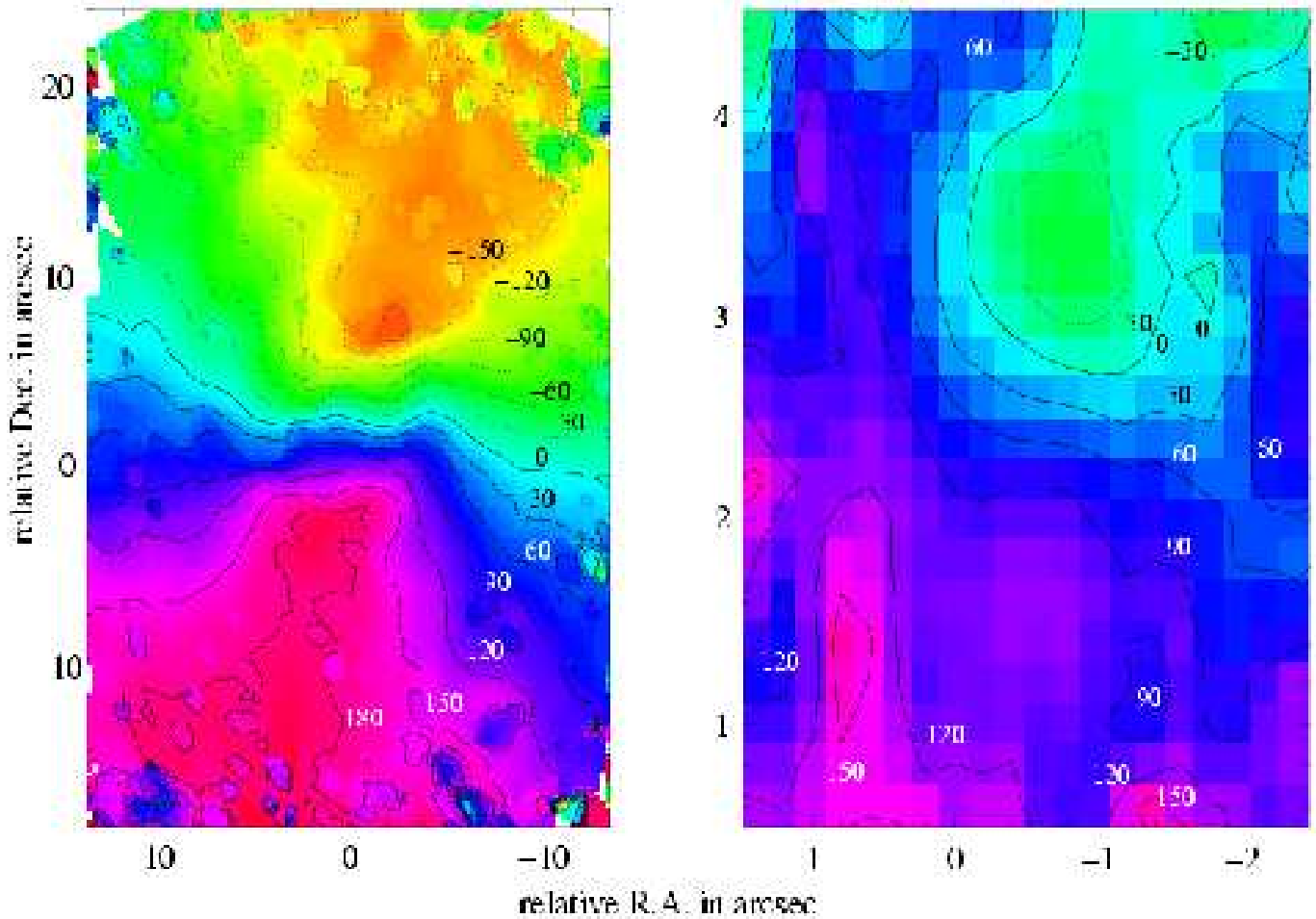


Fig. 5. Iso-velocity diagram of $^{12}\text{CO}(1-0)$ (left panel) and $^{12}\text{CO}(2-1)$ emission (right panel). The $^{12}\text{CO}(2-1)$ emission is observed only in the central part (compare with left panel). The innermost solid contour line is at the systemic velocity and the velocity steps are 30 km s^{-1} .

Parameters	PdBI	PdBI+30m
nucleus:		
$I_{\text{CO}10} [\text{Jy km s}^{-1}]$	17.57	20.30
$V_{\text{CO}10} [\text{K km s}^{-1}]$	1.45	1.86
$N(\text{H}_2) [\text{cm}^{-2}]$	3.18×10^{20}	4.09×10^{20}
$M_{\text{H}_2}^{\text{CO}10} [M_{\odot}]$	1.05×10^8	1.18×10^8
$M_{\text{H}_2+\text{He}}^{\text{CO}10} [M_{\odot}]$	1.43×10^8	1.60×10^8
disk:		
$I_{\text{CO}10} [\text{Jy km s}^{-1}]$	223	485
$V_{\text{CO}10} [\text{K km s}^{-1}]$	0.83	2.04
$N(\text{H}_2) [\text{cm}^{-2}]$	1.86×10^{20}	4.47×10^{20}
$M_{\text{H}_2}^{\text{CO}10} [M_{\odot}]$	6.07×10^7	1.29×10^8
$M_{\text{H}_2+\text{He}}^{\text{CO}10} [M_{\odot}]$	8.26×10^7	1.74×10^8
$M_{\text{gas}}^{\text{CO}10} [M_{\odot}]$	2.04×10^9	2.13×10^9
dynamical mass:		
$M_{\text{dyn}}^{\text{CO}10} [M_{\odot}]$		3.5×10^{10}
$M_{\text{H}_2} [M_{\odot}]$	1.44×10^9	(Mirabel & Sanders, 1988)

Table 4. Results of IRAM PdBI and PdBI+30m telescope.

The values are also apparent from the maps in Fig. 3 (see caption). The $^{12}\text{CO}(2-1)/^{12}\text{CO}(1-0)$ ratio is best determined on

the nucleus with a value close to unity. The deconvolved source size in the $J=2-1$ line emission is 1.4 ± 0.3 arcsec. This results in a $^{12}\text{CO}(2-1)$ line flux of 55.7 Jy km/s in the 3 mm beam and a $^{12}\text{CO}(2-1)/^{12}\text{CO}(1-0)$ line ratio of 0.9 ± 0.1 . This ratio is typical of moderately dense and warm ($n_{\text{H}_2} > 10^4 \text{ cm}^{-3}$, $T_{\text{kin}} \sim 30 \text{ K}$), optically thick molecular clouds if a small contribution from the cosmic microwave background is taken into account as well (see Eckart et al. 1990, García-Burillo et al. 1993). For the weak and extended line emission along the bar, we find an off-nuclear $^{12}\text{CO}(2-1)/^{12}\text{CO}(1-0)$ ratio of 0.2 ± 0.1 . This is indicative of a dominant contribution of cold ($T_{\text{kin}} < 10 \text{ K}$) or sub-thermally ($n_{\text{H}_2} < 10^{-3} \text{ cm}^{-3}$) excited molecular gas.

3.5. Comparison with results at other wavelengths

It is interesting to compare our results achieved through observations of $^{12}\text{CO}(1-0)$ and $^{12}\text{CO}(2-1)$ emission with observational results at other wavelengths. Laine et al. (2006) carried out 20 cm and 3.5 cm wavelength radio continuum observations with the VLA and compare the results with the NIR data of H_2 and Bry from Kotilainen et al. (2000). In the radio and NIR they find a central point-like component and a circum-

nuclear ring. Both source components are very consistent with our observations. The "jet", which is represented as a connection between the nucleus and the circumnuclear ring at 3.5 cm, along the major axis of the galaxy, has no counterpart in our observations.

4. Modeling the CO distribution

In the following section we describe the model used to analyze the data obtained with the IRAM telescopes, then derive the rotation curve and the possible shape of the gaseous orbits.

4.1. The model

The inner 200 pc of NGC 6574 show clear deviations from pure circular motions. To analyze the complex kinematics, we modeled the data with 3DRings similar to the approach of Krips et al. (2005), Pott et al. (2004), and Schinnerer et al. (2000b; see Appendix B therein). With 3DRings only fully symmetric structures can be modeled (i.e., no lopsidedness). The model subdivides the disk into many individual (circular or elliptical) orbits of molecular gas, which lie on the (possibly tilted) plane. With the 3DRings program we investigate the kinematical imprint of (warped) rotating gas.

We model non circular motions with 3DRings via elliptical orbits with changing position angles characterizing gas motions in a bar. The inclination, position angle, and shape of the rotation curve for the overall galaxy were held fixed. Each fitting process was started at large radii and successively extended toward the center. In each case we tried several start setups that all converged to similar (best) solutions with mean deviations from the data of less than about 10 km s^{-1} and 0.1 arcsec for each radius and velocity in the p-v diagrams and 10° in the position angle of the mapped structures. The best decompositions were achieved using a systemic velocity of $v_{\text{sys}} = 43.75 \text{ km s}^{-1}$ in agreement with the derived position velocity diagrams shown in Fig. 4 (see also spectra and channel maps in Figs.1 and 2). The revised best-fit parameters were obtained by comparing the result with the observed PdBI+30m data and tuning the parameters until the match is optimal. We derived an inclination of $45^\circ \pm 10^\circ$ and position angle of $165^\circ \pm 10^\circ$ for the galactic disc in space. In Fig. 7 we show the intensity distribution and rotation curve and in Fig. 8 the ellipticity ϵ and the position angle of the elliptical bar orbits as a function of radius that we used to model the $^{12}\text{CO}(1-0)$ line emission data. The position angle is counted from north to east with respect to the northern part of the inclination axis. This is represented by the dashed line in Fig. 6.

As a result of the modeling we find:

- 1) The rotation curve is basically flat until a radius of at least $1''$ (this is the resolution limit of the observation and of the 3DRings model.) This results in an enclosed mass at this radius of about $2.3 \times 10^9 M_\odot$.
- 2) Starting with almost circular orbits at $20''$ to $30''$ radius, the ellipticity drops to values of $\epsilon \sim 0.2$ ranging in position angles from $\sim 50^\circ$ to $\sim 90^\circ$ approaching the bar position angle in our data (see also the value of $\sim 105^\circ$ given by Sakamoto et al. 1999ab).

- 3) The model requires a constant disk contribution over the entire modeled area with a radius of up to $30''$. An increased central flux component starts at a radius of about $10''$ and then sharply peaks at the center with a value about a factor of 3.0 higher than the disk component. The FWHM of the nuclear component is $\sim 1.5''$; i.e. it is just resolved, as shown also in the maps in Fig. 3.

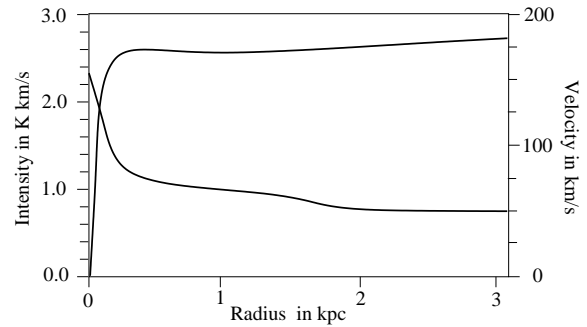


Fig. 7. Intensity distribution and rotation curve as a function of radius as used for modeling the $^{12}\text{CO}(1-0)$ line emission data.

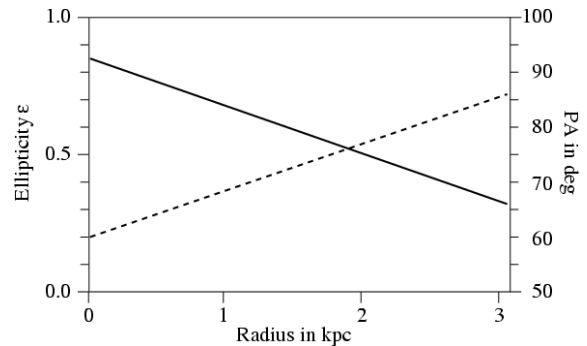


Fig. 8. The ellipticity ϵ (dashed line) and the position angle (full line) of the elliptical bar orbits as a function of radius as used for modeling the $^{12}\text{CO}(1-0)$ line emission data.

5. Computation of the torques

5.1. Near infrared images

We used the near-infrared images kindly made available by J. Reunanen. The JHK images have been obtained by Kotilainen et al. (2000) at UKIRT under $0.6\text{-}0.7''$ seeing and a field of view of $70''$. The H band image is superposed on the CO contours in Fig. 9. There is a very good correspondence between the NIR image and the CO(1-0) contours, indicating that the molecular gas is well aligned along the bar and nuclear bar in NGC 6574. However, a slight phase shift can be noticed, with the gas on the leading side. The nuclear bar is about $8''$ (or 1.2 kpc) in diameter, while the main bar is $20''$ (or 3.2 kpc) in diameter.

The color J-H image is also compared with the CO emission in Fig. 10. It reveals a spiral structure emerging of the main bar. Also, the correlation with the CO distribution is evident. The spiral arms in the CO emission wind up in a pseudo-ring,

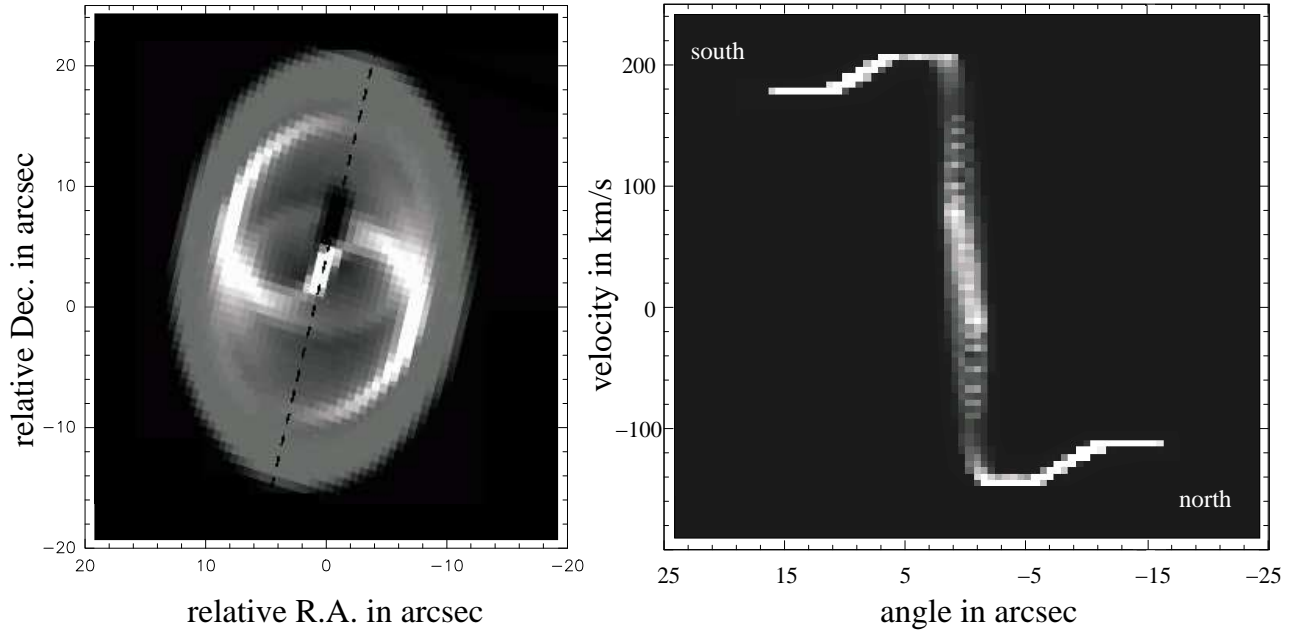


Fig. 6. Integrated intensity map and position velocity diagram along the major axis for the modeled $^{12}\text{CO}(1-0)$ emission. The dashed line at $\text{PA} = 165^\circ$ indicates the position of the major axis of NGC 6574. The position-velocity diagram was obtained as a cut made through the data cube at this position angle.

conspicuous in $\text{H}\alpha$ (Gonzalez-Delgado et al. 1997) and in Bry (Kotilainen et al. 2000). This star-formation ring is likely to correspond to the UHR resonance of the primary bar. Indeed, in most studied galaxies, as shown by simulations and confrontation with observations, the bar ends up near its UHR resonance.

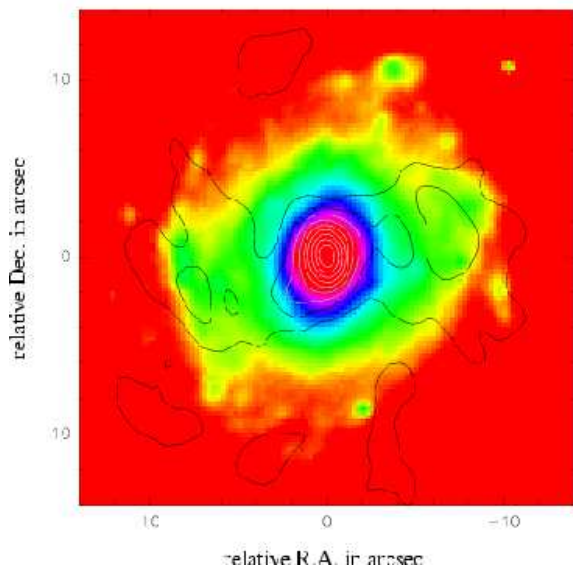


Fig. 9. $\text{CO}(1-0)$ linear contours (1.7 to 17 by 1.7 Jy/beam) superposed on the near-infrared H image, from Kotilainen et al. (2000), in logarithmic levels. The CO emission is aligned along the bar of $\text{PA} = 105^\circ$ and also possibly with the nuclear bar, inside a radius of $3''$.

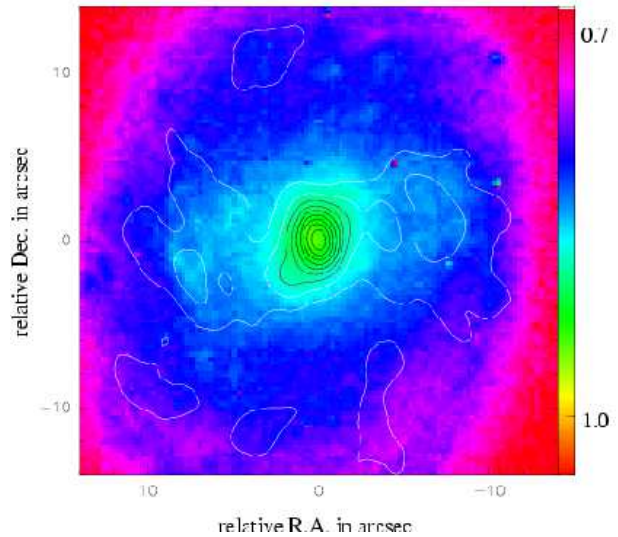


Fig. 10. $\text{CO}(1-0)$ linear contours (1.7 to 17 by 1.7 Jy/beam) superposed on a color image in the near-infrared J-H, from Kotilainen et al. (2000), in logarithmic levels. The CO emission follows a spiral structure, which winds up in a pseudo ring.

5.2. Evaluation of the gravitational potential

As described in previous papers (e.g. Garcia-Burillo et al. 2005), we assume that the NIR images can give us the best approximation for the total stellar mass distribution because it is less affected by dust extinction or by stellar population biases. We here recall the essential definitions and assumptions.

The H image was first deprojected according to the angles $\text{PA} = 165^\circ$ and $i = 45^\circ$. We did not deproject the bulge separately, since we do not know its actual flattening, and the galaxy

- a late type (Sbc) - does not make a large contribution. The image is, however, completed in the vertical dimension by assuming an isothermal plane model with a constant scale height, equal to $\sim 1/12$ th of the radial scale length of the image. The potential is then derived by a Fourier transform method, assuming a constant mass-to-light (M/L) ratio. The M/L value is selected to retrieve the observed CO rotation curve. The axisymmetric part of the model, fitted by parametric functions, is then derived to find the proper frequencies, as shown in Fig. 11. The rotation curve agrees within the uncertainties of the data (Figs. 4) with the rotation curve shown in Fig. 7, which was derived while modeling the CO data alone.

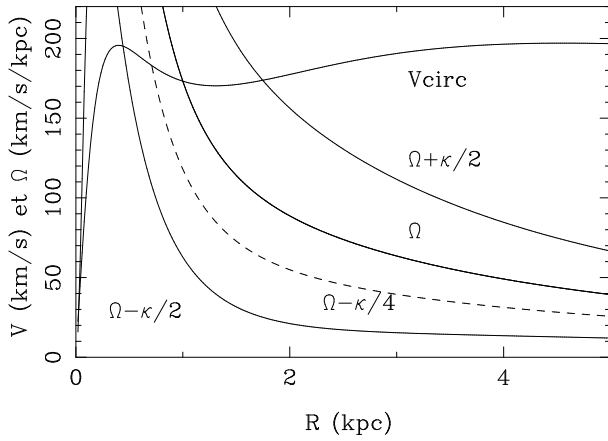


Fig. 11. Rotation curve and derived frequencies Ω , $\Omega - \kappa/2$ and $\Omega + \kappa/2$, for NGC 6574.

For the non-axisymmetric part, the potential $\Phi(R, \theta)$ is then decomposed in the different m -modes:

$$\Phi(R, \theta) = \Phi_0(R) + \sum_m \Phi_m(R) \cos(m\theta - \phi_m(R))$$

where $\Phi_m(R)$ and $\phi_m(R)$ represent the amplitude and phase of the m -mode.

The strength of the m -Fourier component, $Q_m(R)$, is defined as $Q_m(R) = m\Phi_m/R|F_0(R)|$, i.e. by the ratio between tangential and radial forces (e.g. Combes and Sanders, 1981). The strength of the total non-axisymmetric perturbation is defined by

$$Q_T(R) = \frac{F_T^{max}(R)}{F_0(R)}$$

where $F_T^{max}(R)$ represents the maximum amplitude of the tangential force and $F_0(R)$ is the mean axisymmetric radial force. Fig. 12 displays these values as a function of radius for NGC 6574. A main bar can be seen clearly, together with an asymmetry towards the center. The lopsidedness has a correspondence in the gas morphology described in Section 3. The bar is regular in phase, but its strength is relatively modest.

5.3. Evaluation of gravity torques

After having calculated the forces per unit mass (F_x and F_y) from the derivatives of $\Phi(R, \theta)$ on each pixel, the torques per

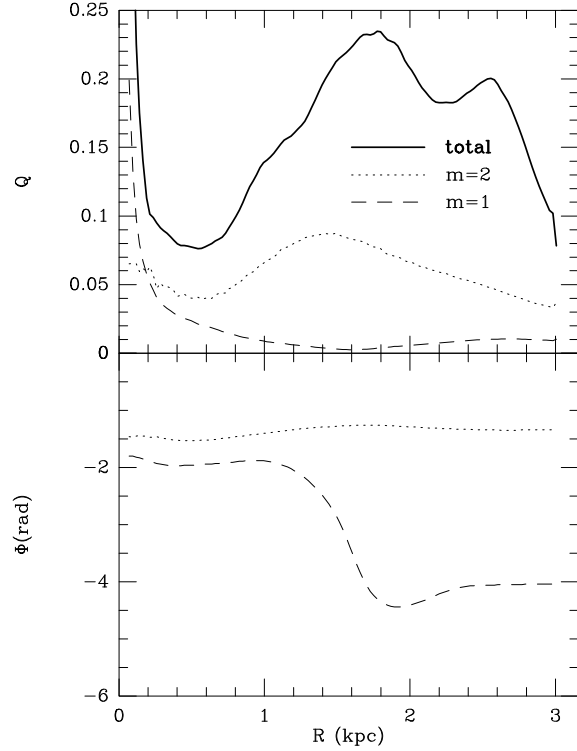


Fig. 12. Strengths (Q_1 , Q_2 , and total Q_T) and phases (ϕ_1 and ϕ_2) of the $m = 1$ and $m = 2$ Fourier components of the stellar potential inside a field of $38''$ in diameter ($r < 3\text{kpc}$). Note the constant phase of the bar.

unit mass $t(x, y)$ can be computed by

$$t(x, y) = x F_y - y F_x .$$

The torque map is oriented according to the sense of rotation in the plane of the galaxy. The combination of the torque map and the gas density $\Sigma(x, y)$ map then allows derivation of the net effect on the gas, at each radius. The gravitational torque map weighted by the gas surface density $t(x, y) \times \Sigma(x, y)$, normalized to its maximum value, is shown in Fig. 13.

To estimate the radial gas flow induced by the torques, we first computed the torque per unit mass averaged over the azimuth, using $\Sigma(x, y)$ as the actual weighting function, i.e.

$$t(R) = \frac{\int_{\theta} \Sigma(x, y) \times (x F_y - y F_x)}{\int_{\theta} \Sigma(x, y)} .$$

By definition, $t(R)$ represents the time derivative of the specific angular momentum L of the gas averaged azimuthally, i.e., $t(R) = dL/dt|_{\theta}$. To derive non dimensional quantities, we normalized this variation in angular momentum per unit time to the angular momentum at this radius and to the rotation period. We then estimated the efficiency of the gas flow with the average fraction of the gas specific angular momentum transferred in one rotation (T_{rot}) by the stellar potential, as a function of radius, i.e., by the function $\Delta L/L$ defined as

$$\frac{\Delta L}{L} = \frac{dL}{dt} \Big|_{\theta} \times \frac{1}{L} \Big|_{\theta} \times T_{rot} = \frac{t(R)}{L_{\theta}} \times T_{rot}$$

where L_θ is assumed to be well represented by its axisymmetric estimate, i.e., $L_\theta = R \times v_{rot}$. The $\Delta L/L$ curves for NGC6574, derived from the CO(1–0) or the CO(2–1) gas, are displayed in Fig. 14.

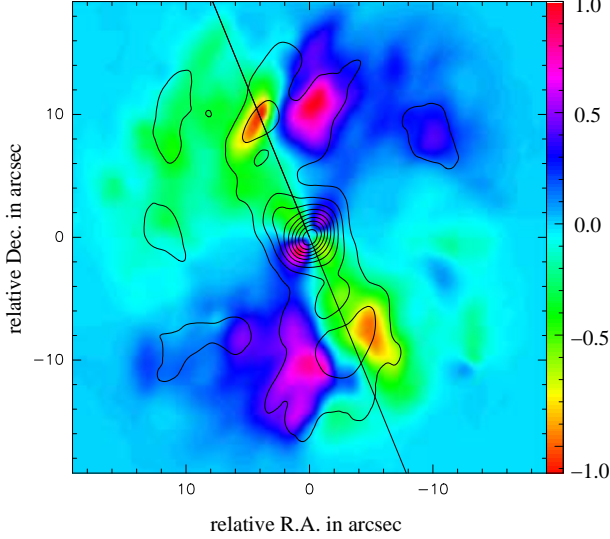


Fig. 13. The CO(1–0) contours are overlaid onto the gravitational torque map ($t(x,y) \times \Sigma(x,y)$), as defined in the text) in the center of NGC 6574. The deprojected torque map (grey/color scale) is normalized to the maximum absolute value of the torques. The derived torques change sign as expected in a *butterfly* diagram, delineating four quadrants. The orientation of quadrants follow the bar orientation in NGC 6574. In this deprojected picture, the major axis of the galaxy is oriented parallel to the abscissa. The inclined line reproduces the mean orientation of the bar (PA= 105° on the projected image).

5.4. Results and discussion

We show in Fig. 13 that the derived torques change sign following a characteristic 2D *butterfly* pattern. The CO contours clearly reveal that the majority of the gas at $r \sim 0.5$ -1.5 kpc is offset from the bar on the leading edge where the torques are negative. The rotation sense in the galaxy is counterclockwise, and the spiral structure is trailing. Towards the center ($r < 400$ pc), however, the dominating torques are positive. Indeed, the average value of dL/L per rotation over 0-400pc is -0.005, and over 400-1500pc is 0.1.

The interpretation of these results can be done in the classical scenario of angular momentum transfer in barred galaxies. The main bar, 1.6 kpc in radius, ends in a pseudo-ring at its ultra-harmonic resonance (UHR), where its pattern speed equals $\Omega - \kappa/4$. According to Fig. 11, we can then derive the probable pattern speed of ~ 60 km/s/kpc. Its co-rotation should then be around 2.8kpc. Since the rotation curve gradient is quite strong in the center, as revealed by the CO kinematics, there must be an ILR in the circumnuclear region, which might correspond to the high gas concentration there, at $r < 600$ pc. The ILR is usually the site of high gas concentration in a ring. A

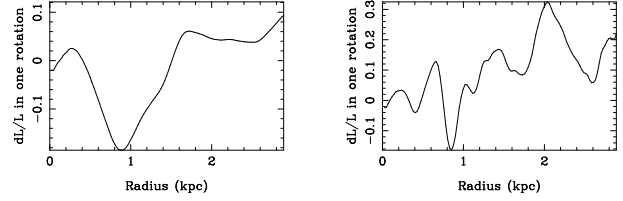


Fig. 14. The torque, or more precisely the fraction of the angular momentum transferred from/to the gas in one rotation dL/L , plotted for CO(1-0) (left), and CO(2-1) (right). The curve is noisier for the CO(2-1) line due to a lower sensitivity at 230 GHz. Both curves, however, show negative torques around 1 kpc radius (more precisely from 0.4 to 1.5kpc for the CO(1-0)).

suggestion of such a nuclear ring has been given in Section 3, by the two prominent concentrations of CO in the major axis p-v diagrams. It is obvious that the CO emission is not peaked in the very center, around systemic velocity, but corresponds to an elongated nuclear ring, with highly non-circular motions, at a radius of about 130pc. With the pattern speed of ~ 60 km/s/kpc, two ILR must exist, as suggested by the rotation curve of Fig. 11. However, this indication is only derived from the $\Omega - \kappa/2$ curve with the epicyclic approximation, which is not valid for a strong bar. The effective curve is lower, and the ILR might be expected between 30 and 900 pc. Moreover, if a nuclear ring exists, it is likely to be elongated, corresponding to the range of radii usually found in numerical simulations. In addition, the near infrared images give a hint of a nuclear bar, but this is not certain. This nuclear bar is expected from theory to decouple in such conditions, inside the nuclear ILR ring.

The gas flow towards the center is taken just in the act, at the present epoch. The flow rate is not very high, due to a bar that is relatively weak (see Fig. 12). But the gas flow already has a visible consequence: a high concentration of molecular gas towards the center, which must be recent, since the center is not the location of any starburst (no peak in Br γ or H α).

The maps presented here lack spatial resolution to determine unambiguously whether the gas is stalled at the ILR of the main bar, or if it could be still driven inwards due to a nuclear bar. In either case, we conclude that we are seeing the gas inflow fueling the center, which soon will feed the AGN nucleus. A possibility is that the feeding is intermittent, since the gas flows induced by gravity torques in the very center ($r < 400$ pc) have a very short time scale of $t_{dyn} \sim 12$ Myr.

6. Discussion and summary

In this paper we present the analysis of subarcsec-resolution PdBI observations of molecular gas in the Seyfert 2 NGC 6574 with a short spacing correction derived from IRAM 30m telescope observations. Our data complements the analysis made by Sakamoto et al. (1999ab) for $^{12}\text{CO}(1-0)$ observations and expands the analysis with observations of the $^{12}\text{CO}(2-1)$ line emission. The successful descriptive modeling of the disk dynamics with elliptical bar orbits corroborates the hypothesis that the molecular gas is strongly influenced by the stellar bar-

like potential located within a more extended molecular gas disk (Laine et al. 2006, Kotilainen et al. 2000).

Within the NUGA sample, a wide variety of morphologies and dynamics are observed (see introduction and e.g. García-Burillo et al. 2005). With the exception of a nuclear warp, NGC 6574 shows all of these attributes. But even a nuclear warp cannot be excluded as it only becomes apparent at the highest linear resolution (sub-100 pc), which can only be achieved for the closest nuclei (e.g. NGC 1068 and NGC 3227; e.g. Schinnerer et al. 2000a). In most cases, there is very little evidence that any of the observed features can be uniquely linked to the activity of the nucleus. In some cases (NGC4826: García-Burillo et al. 2003, NGC7217: Combes et al. 2004) the detailed analysis of the observed source properties even appear to rather inhibit than to support fueling of the nuclear region.

Contrary to the majority of NUGA galaxies studied so far, there is clear evidence in NGC6574 of gas inflow on a very small scale, of a few hundred parsec, where we find CO emission down to our spatial resolution. The gas appears to accumulate at this central location, and the inflow must be recent, since there is still no nuclear starburst observed. The CO position-velocity diagrams reveal a hint of an elongated nuclear ring there, which would be the ILR of the main bar. Our resolution does not allow us to go further to determine whether the gas is stalled at this ILR ring or driven inwards to feed the AGN through a nuclear bar.

In either case, our result is consistent with the previous finding that low-luminosity AGN (the NUGA sample includes Seyferts and LINERs) do not require any efficient fueling to sustain their luminosity (see e.g. Ho 2003). It is also unclear which processes dominate the infall of gas into the region with radii that are beyond our current angular resolution i.e. linear scales of less than ~ 100 pc. Nuclear bars (Shlosman et al. 1989), lopsidedness or $m = 1$ instabilities (García-Burillo et al. 2000), and nuclear spiral density waves (Englmaier & Shlosman 2000) provide processes that enable the gas infall into the central few parsecs. In the case of NGC 6574, both the $^{12}\text{CO}(1-0)$ and the $^{12}\text{CO}(2-1)$ integrated line-intensity maps consistently show evidence of a weak extension toward the southeast. This may be interpreted as indicating lopsidedness and may therefore be responsible for transporting molecular gas into the central 100 pc. If, however, none of the above-mentioned mechanisms are efficient, then as an alternative, viscosity may support such a transport.

How viscosity may be responsible for transporting gas toward the center of such disks has been shown by Duschl et al. (2000). The authors suggest that viscosity within these gaseous disks may provide an efficient AGN fueling mechanism. However, viscosity could also counteract low-gravity torques on the gas. García-Burillo et al. (2005) discuss the details of viscosity effects versus gravity torques to drive AGN fueling. The authors find that such a counteraction may occur if it acts on a nuclear ring of high gas-surface density contrast and a few 100 pc size. Whether only one of these mechanisms of different efficiency or a combination of them usually accounts for the gas infall is still unknown. García-Burillo et al. (2005) propose an evolutionary scenario in which gravity torques and

viscosity act in concert to produce recurrent episodes of activity during the typical lifetime of any galaxy.

Alternatively, the timescales for fueling on the few 100 pc scale and the onset of activity are so different that both cannot be observed simultaneously (see e.g. Combes 2004). In that case detailed investigations of nuclear gas fueling that drives the AGN accretion and possibly the star formation process in the very center of the nuclear star cluster have to resort to studies of the molecular and atomic gas dynamics on size scales of less than 10 pc. This could become possible with the high sensitivity and angular resolution that will be provided by ALMA.

Acknowledgements. Part of this work was supported by the German *Deutsche Forschungsgemeinschaft*, DFG project number SFB 494. We thank the IRAM staff from the Plateau de Bure and from Grenoble for carrying out the observations and help provided during the data reduction, especially to J. M. Winters.

References

- Baker, A. J., Jogee, S., Sakamoto, K., Scoville, N.Z., 2003, ASPC 290, 479
- Binney, J. & Tremaine, S., Galactic dynamics, Princeton, NJ, Princeton University Press, 1987, p. 747
- Clark, B. G., 1980, A&A 89, 377
- Combes, F., & Sanders, R. H. 1981, A&A, 96, 164
- Combes, F., 2004 IAU Symp 222, 383
- Combes, F., García-Burillo, S., Boone, F., et al.: 2004, A&A, 414, 857
- Duschl, W. J., Strittmatter, P. A., Biermann, P. L., 2000, A&A 357, 1123
- Eckart, A., Downes, D., Genzel, R., et al.: 1990, ApJ 348, 434
- Elmegreen, B. G., Elmegreen, D. M., Brinks, et al., 1998 ApJ 503, L119
- Englmaier, P., & Shlosman, I. 2000, ApJ, 528, 677
- Friedli, D., Martinet, L., 1993, A&A 277, 27
- García-Burillo, S., Guélin, M., Cernicharo, J. 1993, A&A, 274, 123
- García-Burillo, S., Sempere, M. J., Combes, F., Hunt, L. K., & Neri, R. 2000, A&A, 363, 869
- García-Burillo, S., Combes, F., Hunt, L. K., et al.: 2003, A&A, 407, 485
- García-Burillo, S., Combes, F., Schinnerer, E., Boone, F., Hunt, L. K. 2005, A&A, 441, 1011
- Gonzalez Delgado, R. M., Perez, E., Tadhunter, C., Vilchez, J. M., Rodriguez-Espinosa, J.M.: 1997 ApJS 108, 155
- Greve, A., Panis, J.-F., Thum, C., 1996, A&AS 115, 379
- Guilloteau, S., & Lucas, R. 2000, in ASP Conf. Ser.: Imaging at Radio through Submillimeter Wavelengths, ed. J. G. Mangum & S. J. E. Radford, vol. 299
- Kotilainen, J. K., Reunanen, J., Laine, S., Ryder, S. D. 2000, A&A, 353, 834
- Heller, C. H., Shlosman, I 1994, ApJ, 424, 84
- Heckman, T. M., Smith, E. P., Baum, S. A. et al. 1986, ApJ, 311, 526
- Ho, L.C., 2003 ASPC 290, 379
- Kormendy, J., & Bender R. 1999, ApJ, 522, 772
- Krips, M., Eckart, A., Neri, R., et al.: 2005, A&A, 442, 479
- Laine, S., Kotilainen, J. K., Reunanen, J., Ryder, S. D., Beck, R. 2006, AJ 131, 701
- Martini, P., & Pogge, R. W. 1999, AJ, 118, 2646
- Meixner, M., Puchalsky, R., Blitz, L., Wright, M., Heckman, T., 1990, ApJ 354, 158
- Mirabel, I.F. & Sanders, D. B. 1988, A&A, 335, 104-121
- Pott, J.-U., Hartwich, M., Eckart, A., et al.: 2004, A&A, 415, 27

- Regan, M. W., & Mulchaey, J. S. 1999, *AJ*, 117, 2676
- Sakamoto, K., Okumura, S. K., Ishizuki, S., Scoville, N. Z. 1999a, *ApJ*, 525, 691
- Sakamoto, K., Okumura, S. K., Ishizuki, S., Scoville, N. Z. 1999b, *ApJS* 124, 403
- Schinnerer, E., Eckart, A., Tacconi, L. J. et al. 2000a, *ApJ*, 533, 850
- Schinnerer, E., Eckart, A., & Tacconi, L. J. 2000b, *ApJ*, 533, 826
- Shlosman, I., Frank, J., & Begelman, M. C. 1989, *Nature*, 338, 45
- Solomon, . & Barrett 1991, 1991, *IAUS* 146, 235
- Tacconi, L. J., Gallimore, J. F., Genzel, R., Schinnerer, E., Downes, D., 1997 *Ap&SS* 248, 59
- Vila-Vilaró, B., Taniguchi , Y., & Nakai, N. 1998, *AJ*, 116, 1553